Calcium-vesicles perform active diffusion in the sea urchin embryo during larval biomineralization

Mark R. Winter[1], Miri Morgulis[1], Tsvia Gildor[1], Andrew R. Cohen[2] and *Smadar Ben-Tabou de-Leon[1]

[1]Marine Biology Department, Charney School of Marine Sciences, the University of Haifa, Haifa, Israel

[2]Drexel University, PA, USA

*Author of correspondence, e-mail: sben-tab@univ.haifa.ac.il phone: +972-52-6135770

Calcium-vesicle diffusion in biomineralization

ABSTRACT (<300 words)

Biomineralization is the process by which organisms use minerals to harden their tissues and provide them with physical support. Biomineralizing cells concentrate the mineral in vesicles that they secret into a dedicated compartment where crystallization occurs. The dynamics of mineral-vesicle motion and the molecular mechanisms that regulate it, are not well understood. Sea urchin larval skeletogenesis provides an excellent platform for the analyses of vesicle kinetics. Here we used calcein labeling and lattice light-sheet microscopy to investigate the three-dimensional (3D) vesicle dynamics in control sea urchin embryos and in Vascular Endothelial Growth Factor Receptor (VEGFR) inhibited embryos, where skeletogenesis is blocked. We developed computational tools for displaying 3D-volumetric movies and for automatically quantifying vesicle dynamics in the different embryonic tissues. Our findings imply that calcium vesicles perform an active diffusion motion in all the cells of the embryo. This mode of diffusion is defined by the mechanical properties of the cells and the dynamic rearrangements of the cytoskeletal network. The diffusion coefficient is larger in the mesenchymal skeletogenic cells compared to the epithelial ectodermal cells, possibly due to the distinct mechanical properties of the two tissues. Vesicle motion is not directed toward the biomineralization compartment, but the vesicles slow down when they approach it, and probably bind for mineral deposition. Under VEGFR inhibition, vesicle volume increases and vesicle speed is reduced but the vesicles continue in their diffusive motion. Overall, our studies provide an unprecedented view of calcium vesicle 3D-dynamics and illuminate possible molecular mechanisms that control vesicle dynamics and deposition.

Authors summary (150-200 words)

Biomineralization is a widespread, fundamental process by which organisms use minerals to harden their tissues. Mineral bearing vesicles were observed in biomineralizing cells and believed to play an essential role in biomineralization, yet little is known about their three-dimensional (3D) dynamics. Here we quantify 3D-vesicle-dynamics during skeleton formation in sea urchin larvae, using lattice-light-sheet microscopy. We discover that calcium vesicles perform an active diffusive motion in both calcifying and non-calcifying cells of the embryo. The motion of the vesicles in the calcifying skeletogenic cells, is not directed toward the biomineralization compartment and has a diffusion coefficient of ~$0.01\mu m^2/sec$ and average speed of $\sim 0.09\mu m/sec$. The inhibition of Vascular Endothelial Growth Factor Receptor (VEGFR) that blocks skeletogenesis, increases vesicle volume and decreases vesicle speed but doesn't change the diffusion mode in the embryo cells. Our studies reveal the diffusive motion of mineral bearing vesicles and have implications on basic and translational research.

Biomineralization; biophysics; Lattice light sheet microscopy; vesicles trafficking; active diffusion; sea urchin; VEGF

Introduction

Organisms from the five kingdoms of life use different minerals to harden their tissues and gain protection and physical support[1]. The ability of the cells to control the time and place of crystal nucleation as well as crystal orientation, elasticity and stiffness is beyond the state-of-the art of human technologies[2-4] and inspired the design of biomimetic systems[5-7]. Biomineralization is thought to have evolved independently and rapidly in different phyla, through the use of preexisting components and the evolution of specialized biomineralization proteins[8, 9]. The biomineralized skeletons, teeth and shells, constitute the fossil record that carry the information on the evolution of life on earth. Thus, revealing the cellular and molecular control of the biomineralization process has been the desired goal of both fundamental and applied researchers in the fields of biology, chemistry, geology and material sciences[1, 8-10].

Within the variety of minerals used and phylum specific proteins, a common design of mineral uptake and deposition emerges from various studies: the mineral enters the cells through endocytosis of extracellular fluid[11, 12]. The mineral is then concentrated and maintained in an amorphous phase in intracellular vesicles until the vesicles are deposited into a dedicated compartment where crystallization occurs[13]. The biomineralization compartment provides a highly regulated environment for crystal nucleation and growth. The molecular mechanisms that regulate the accumulation and trafficking of mineral vesicles and those that control vesicle secretion into the biomineralization compartment, are not well understood.

Sea urchin larval skeletogenesis is an excellent system for investigating mineral uptake and deposition within a relatively small (~100μm) and transparent embryo, which is easy to manipulate[11, 14-21]. The sea urchin skeleton is made of two rods of calcite termed “spicules” generated by the skeletogenic mesodermal cells[18, 22]. The skeletogenic cells fuse and arrange in a ring with two lateral symmetrical cell clusters. In those lateral clusters the skeletogenic cells form a tubular compartment into which calcium-carbonate is deposited to make the calcite spicules[16, 20, 21]. The uptake of calcium from the blastocoel fluid occurs through endocytosis, as was shown through a series of experiments[11, 14, 15]: Electron microscope images of the skeletogenic cells show cell membrane invagination that forms an inner pocket of about 1μm filled with blastocoel fluid[11]. This pocket then separates from the cell membrane and forms an intracellular vesicle with a similar size (~1μm)[11, 14, 15]. Calcium vesicle movement was tracked manually and the vesicles seem to barely move within the skeletogenic and ectodermal cells[15]. Calcium and carbonate are eventually concentrated in the vesicles in the form of

amorphous calcium-carbonate (ACC)[11, 14, 15, 23], which is deposited into the biomineralization compartment where crystallization occurs[14, 20, 24, 25].

The regulation of endocytosis and vesicular transport between membrane-bound cellular compartments were intensively studied in other systems[26, 27]. The observed size of the pocket and vesicles (~1µm) suggests that this endocytosis process is most likely macropinocytosis ("cell drinking"), and not receptor/clathrin mediated endocytosis (upper limit of ~200nm)[26] or caveolin mediated (upper limit of ~80nm)[28]. Macropinocytosis is an actin-dependent process that initiates from surface membrane ruffles that give rise to large endocytic vacuoles called macropinosomes[29]. The macropinosomes go through a maturation process that involves shrinking and coating with various membrane-bound proteins[30, 31]. Some of the membrane-bound proteins could be motor proteins like dynein or kinesin that actively transport vesicles along the microtubules in the cells[32, 33]. Alternatively, the vesicles can perform a diffusive motion that is constrained by the cellular organelles and affected by the dynamic remodeling of the cytoskeleton network within the cell[34-37]. This mode of vesicle diffusion within the cells is called "active diffusion" to distinguish it from thermal diffusion[34-37]. Possibly, some of the molecular mechanisms that regulate macropinosomes shrinking and transport are used by the skeletogenic cells to concentrate the calcium and carbonate they uptake from the blastocoel and transfer it into the biomineralization compartment.

The molecular control of sea urchin skeletogenesis has been intensively studied resulting in a state-of-the-art model of the gene regulatory network (GRN) that controls skeletogenic cell fate specification[17, 18, 38-40]. A key control gene in this GRN encodes the Vascular Endothelial Growth Factor Receptor (VEGFR)[17, 39-41],[77] that in vertebrates regulates the formation of blood vessels (vascularization) and the sprouting of new blood vessels from existing ones (angiogenesis)[42]. VEGFR is exclusively expressed in the sea urchin skeletogenic cells, and its inhibition by either genetic manipulation or using the VEGFR specific inhibitor, axitinib, distorts skeletogenic cell migration and completely blocks spicule formation[17, 39, 41],[77]. We previously studied the cellular and molecular machinery activated by the VEGF pathway during sea urchin skeletogenesis and revealed multiple parallels to the regulation of vertebrate vascularization[17]. The similarities are observed both in the upstream gene regulatory network, in the downstream effector genes and the cellular processes that VEGF signaling activates. Possibly, sea urchin skeletogenesis and vertebrate vascularization diverged from a common ancestral tubulogenesis program, uniquely co-opted for biomineralization in the echinoderm phylum.

VEGFR inhibition in the sea urchin embryo affects the number of calcium vesicles accumulated in the skeletogenic cells[17]. We previously studied the role of sea urchin VEGF signaling in calcium vesicle accumulation using calcein labeling in live embryos by confocal microscopy[17]. We observed that calcium vesicles are still detected in the sea urchin embryo under VEGFR inhibition. However, when the spicules form in normal embryos the number of vesicles in the skeletogenic cells is higher under VEGFR inhibition compared to normal embryos. Possibly, calcium vesicles accumulate in higher numbers in the skeletogenic cells when VEGF signaling is inactive since the biomineralization compartment doesn't form and vesicles are not deposited. Yet, these measurements were based on two dimensional images, therefore they lack the volumetric information and temporal resolution required for assessing calcium vesicle volume and kinetics in the 3-dimensional (3D) cellular environment. Lattice light-sheet microscopy (LLSM) is a promising technique for the measurement and assessment of the 3D vesicle dynamics in live sea urchin embryos[43].

LLSM is a recent improvement in 3D fluorescence imaging[43]. Light-sheet microscopy (LSM) excites a sample using an excitation objective that is perpendicular to the imaging objective. This excitation along a "sheet" reduces the excitation time for each point in the sample, while maintaining similar resolution to confocal microscopy. Lattice light-sheet techniques extend LSM by using a lattice beam to excite the sample rather than a Gaussian beam. The lattice beam improves the spatial resolution of the excitation, as well as reduces the intensity of excitation on the sample. LLSM techniques produce high spatial and temporal resolution images, while avoiding the phototoxicity problems that are common with confocal and standard LSM. The high spatial and temporal resolutions are indispensable for capturing the motion of fast-moving subcellular structures such as the calcium vesicles. In addition, the reduced excitation of the LLSM avoids harming the cells of the embryo allowing for the long-term visualization of calcium dynamics.

The power of LLSM to produce fast high-resolution imaging also presents new challenges for data analysis. Single slice-based visualization often misses important structure in the 3D volume. While full 3D volumetric visualization provides a more comprehensive view of the data, it also requires a deep understanding of the image statistics in order to properly highlight structures of interest. Similar to looking through fog, image noise in 3D volumetric data visualization can obscure the structure unless the visualization parameters are tuned for each dataset. The high throughput of LLSM exacerbates these problems: the microscope can generate gigabytes of image data per minute, requiring high-performance graphics and computer hardware in order to

enable real-time visualization of the datasets. Therefore, manually quantifying cellular and sub-cellular dynamics in tens of 3D movies, each having hundreds of frames, is error-prone and in most cases, practically infeasible.

Automated analysis approaches are highly suitable for handling large 3D LLSM datasets. However, accurate computational analysis of biological image data is also an active area of research and presents additional cross-disciplinary challenges. Quantification of cellular dynamics begins with automatic identification of individual structures of interest in each frame (often referred to as segmentation). After segmentation, a tracking algorithm links the segmented structures frame-to-frame to maintain the "identity" for each object over time. Once tracking is complete, size and motion dynamics can be measured for each object and statistical comparisons can be made. Several software tools have been developed focused on automatic 3D biological image analysis[44-46]. The LEVER package is extensible and supports visualization of the vesicle tracking along with the raw image data for validation of the automated results. LEVER has previously been used for both 2D and 3D cellular dynamics quantification. As part of this work we integrated our segmentation and tracking approaches into LEVER to be used for quantifying 3D calcium vesicle dynamics[47-49].

Here we used LLSM to measure 3D vesicle dynamics in control and VEGFR inhibited sea urchin embryos at the gastrula stage using calcein and membrane labeling. We extended the LEVER software platform to support automatic identification and tracking of calcium vesicles in 3D and to generate interactive volumetric 3D visualization and movie capture. We applied these tools to quantify calcium vesicle dynamics within different embryonic tissues and across experimental conditions. Our studies reveal the typical length and velocity scales and the characteristic motion of calcium vesicles in the sea urchin embryonic cells and illuminate possible molecular mechanisms that control this motion.

Results

Detecting cellular and calcium vesicle dynamics in LLSM

In order to visualize 3D calcium vesicle dynamics in live sea urchin embryos for long periods of time, we used the LLSM at the advanced imaging center at the Janelia research campus[43]. This LLSM setup allows for high temporal resolution of ~40ms per slice and about ~2 sec for 3D embryonic volume of ~40µm[43, 50]. We used green calcein to stain the calcium ions[14] and FM4-64 to mark cell membranes in live sea urchin embryos of the species, *Lytechinus variegatus*

(*L. variegatus*) at different stages of skeletogenesis (Fig. 1A-C)[17]. Calcein is membrane-impermeable and therefore can only enter the cells through endocytosis[11]. To study the effect of VEGF signaling we treated sea urchin embryos with the VEGFR inhibitor, axitinib (Fig. 1D-F). Axitinib is a specific inhibitor of human VEGFR2 that binds to the kinase domain that is highly conserved between human and sea urchin; specifically, the six amino-acids to which Axitinib binds are conserved between human and sea urchin VEGFR[17]. Axitinib treatment results in similar skeletogenic phenotypes to those observed in genetic perturbations of the VEGF gene in *L. variegatus*[39] and particularly, it results in complete skeletal loss (Fig. 1D-F)[17, 39]. Axitinib is dissolved in DMSO and our control embryos were therefore cultured in a similar concentration of DMSO like the axitinib embryos, see Methods for experimental details. Details of all the time-lapses we used in this work are provided in Dataset S1.

Before we further describe our experiments and observations, some methodological limitations must be mentioned. The embryos were grown in calcein until early gastrula stage and then calcein was washed about two hours or more before we could image vesicle dynamics. This time interval after the wash was necessary to eliminate the calcein stain from the cell cytoplasm and blastocoelar fluid so the individual calcein stained-vesicles would be distinct from the background. However, as the blastoceolar fluid was not stained with calcein during the imaging, we were unable to detect live-pinocytosis as well as unstained calcium vesicles that were apparently deposited into the spicules (Fig. 1C). To immobilize the embryos and enable live-imaging for long period of time (>30min), we immersed the embryos in low melting agarose and in this condition the spicule elongation is significantly slower than in free swimming embryos. In other systems, substrate stiffness was shown to regulate cellular behaviors[51],[52], and we need to consider this effect in our interpretation of the data.

4D rendering of the LLSM data reveals rich cellular behaviors and vesicular dynamics

To visualize the 3D structure and motion of the cells and the vesicles in the embryos throughout time, we reconstructed a 3D model from the individual slices and then connected these images over time to produce time-lapse sequences. The datasets are made up of two-channels (calcein and FM4-64) of between 80 to 120 image-slices per time point (frame). Each frame is reconstructed into a 3D volume that spans approximately 40μm of the sea urchin embryo. We present here six representative movies, three of control and three of VEGFR inhibition, that include 200-400 frames separated by time intervals of 3.26-6.12 sec, spanning about 20-30 minutes of cellular and vesicular motion (Fig. 1 and Movies S1-6).

The rendered movies demonstrate the highly dynamic cellular and vesicular motion in the two experimental conditions. At the developmental stages in which we recorded the movies the skeletogenic cells are in close contact with the ectodermal layer[53]. In normal embryos they are in close vicinity to the developing spicule (Fig. 1B,C, 2A) and in both conditions they form clusters and rapidly extend filopodia that contact and fuse between cells[39] (Figs. 1 and 2). We also detect some non-skeletogenic mesenchymal cells that move around individually and are not in direct contact with the ectoderm (Fig. 1A, Sup movie 3). The formation of skeletogenic cell clusters that are bound to the ectoderm in both control and VEGFR inhibition suggests that VEGF-independent ectodermal cues are responsible for the observed skeletogenic adhesion[53].

Vesicle volume is larger in the skeletogenic cells vs. the ectodermal cells and increases under VEGFR inhibition

Next, we wanted to study the effect of VEGFR inhibition on the volume of calcium vesicles within the embryonic cells. To automatically quantify vesicle volume, we identified each vesicle in all frames using the segmentation algorithm discussed in the methods section (Fig. 3A, B). After automated identification of each vesicle, the size of each vesicle can be measured based on the volume of the pixels identified. To differentiate between the skeletogenic cells and the other embryonic territories we manually identified the boundaries of the ectoderm and of the endoderm regions in the first frame of each movie and used this frame for volume statistics (Fig. 3C). As the endoderm region was apparent only in few of the movies, we focused on characterizing the sizes of vesicles in the ectoderm and the skeletogenic cells. In some of the movies the mesodermal region contains a few non-skeletogenic mesodermal cells, but since the movies were focused on clusters of skeletogenic cells, the contribution of the non-skeletogenic cells to our analyses is minor.

Our measurements show that in control embryos, the average volume of calcein stained vesicles in the skeletogenic cells is ~0.4μm^3 while in the ectodermal cells it is significantly smaller, ~0.25μm^3 (Fig. 3D, Dataset S1). Under VEGFR inhibition, the average volume of calcein stained vesicles is higher compared to normal embryos both in the skeletogenic cells and in the ectodermal cells (Fig. 3D, Dataset S1). The average volume of the calcein stained vesicles under VEGFR inhibition is ~0.46μm^3 in the skeletogenic cells and ~0.34μm^3 in the ectodermal cells, an increase of more than 12% in vesicle volume in both tissues. We previously observed an increase in the number of vesicles in the skeletogenic cells under VEGFR inhibition at the time when the spicule forms in normal embryos[17]. The increase in vesicle number and volume might result from the higher level of calcium present in the blastocoel when VEGF signaling is inactive, since

calcium is not sequestered into the spicules and accumulates in the blastocoel and its level is increased in all the cells of the embryo.

Vesicle speed is slower in the skeletogenic cells compared to the ectodermal cells and the directionality is similar in the two tissues.

We wanted to quantify vesicle dynamics in the cells of the sea urchin embryo and study the effect of VEGFR inhibition on vesicle motion. To do that we applied the tracking algorithm we developed previously[49, 54] (see the methods section for details). Tracking maintains the identity of each vesicle over time, allowing instantaneous speed and velocity measurements, frame to frame, for each individual vesicle. Throughout this manuscript we use the term "**speed**" to describe the size of the velocity and the term "**velocity**" to describe the vector-velocity that includes the information of both the size and direction. An example **instantaneous speed** measurement is shown in Figure 4A, the magenta line represents the motion of the vesicle from the previous frame. The vesicle instantaneous speed is the length of the line (distance traveled in a single frame) divided by the time between frames (here, ~6 seconds). An important constraint on the effectiveness of tracking algorithms is the temporal resolution of the imaging relative to the speed of tracked objects. In the case of the calcium vesicles, we discovered that too much motion occurred between frames for effective tracking if the temporal resolution was 15 seconds or more per frame. We therefore only applied the tracking algorithm and motion analyses to movies with temporal resolution less than 15 seconds per frame, that is, 3.26-6.12 seconds per frame (see Dataset S1 for the details of movies that were included in this analysis).

The average instantaneous speed per track of the vesicles in the skeletogenic cells is about 0.09μm/sec in control embryos and is reduced to ~0.08μm/sec in VEGFR inhibition (Fig. 4C, Dataset S1 and methods). A larger difference is observed between the vesicle speed in the skeletogenic cells and in the ectoderm, where the average instantaneous speed per track is 0.07μm/sec in control embryos and reduces to ~0.05μm/sec under VEGFR inhibition. Thus, vesicle volume and speed are larger in the skeletogenic cells compared to the ectodermal cells in both control and VEGFR inhibition (Fig. 3D, 4C, Dataset S1).

Interestingly, the instantaneous speed decreases with VEGFR inhibition while the volume increases in this condition for both the skeletogenic cells and the ectoderm. Despite these clear trends, there is no correlation between vesicle volume and speed throughout the experimental conditions (Fig. S1A, B). The lack of correlation implies that the change of vesicle volume is not related to the change in vesicle motion and is due to different regulation of these quantities in the embryonic cells.

To further characterize vesicle motion, we quantified the directionality of vesicle velocity by measuring the **directionality index**. The directionality index is the ratio between the maximal displacement and the total length of the vesicle track during a time window of one minute (Fig. 4B)[55, 56]. Values close to 1, reflect linear (directed) motion and values close to 0, reflect random motion. The average directionality index in both the skeletogenic and ectodermal cells is about 0.42 and it shows minor changes under VEGFR inhibition (Fig. 4D, Dataset S1). This value is similar to the directionality index measured for endocytic vesicles that guided by molecular motors along microtubules in astrocyte cultures[55, 56]. However, the typical speed of motor-guided vesicles in these cultures and in other systems is much faster (~0.4-0.5μm/sec)[55-57] compared to our measurements (~0.05-0.09μm/sec). Additionally, the motor-guided movement of vesicles along microtubules was shown to be in bursts of directed motion that last ~6-7 seconds followed by a pause for a similar time interval[36, 57]. If that was the case for the calcium vesicles we would have expected to see two peaks of instantaneous speed, a fast-speed peak corresponding to the directed motion and a slow-speed peak corresponding to the pause. However, the distribution of measured instantaneous speed shows only a single peak that corresponds to the relatively slow movement of the vesicles reported above (Fig. S2). The slow instantaneous speed and the lack of two modes of motion suggest that the vesicle motion is not guided by molecular motors along the microtubule network.

The calcium vesicles perform an active diffusion motion in the skeletogenic cells and the ectoderm

In other systems, vesicles were shown to experience a diffusive motion that is not thermal in nature but results from the dynamic remodeling of the cytoskeletal network and the ubiquitous activity of motor proteins that affect every moving object within the cell cytoplasm[36, 37]. This mode of diffusion is called “active diffusion” and is characterized by a larger amplitude (step size) compared to the amplitude of thermally-induced diffusion. Additionally, the diffusion coefficient for active diffusion is independent of particle size, unlike thermal diffusion where the diffusion coefficient decreases with increasing particle size[37]. To test whether the calcium vesicles experience an active diffusion motion we fit a standard diffusion motion model to each track. We plot the mean-square displacement, $\langle \Delta x^2 \rangle$, as a function of time, Δt, and use a linear fit to measure the **diffusion coefficient**[34], $\boldsymbol{D}$, $\langle \Delta x^2 \rangle = D\Delta t$, for each track (Fig. 4E). Mean-square displacement is measured by taking the squared sum of path-lengths (e.g. the lengths of magenta line segments in Fig. 4B) for each vesicle track. Most of the data fit well within this model, that is, $R^2 \geq 0.8$ for 90% of the tracked vesicles (Fig. 4F). The average diffusion coefficient is

D~0.01$\mu m^2/sec$ in the skeletogenic cells and is not affected by VEGFR inhibition (Fig. 4E, Dataset S1). In the ectoderm the diffusion coefficient is smaller, D~0.008$\mu m^2/sec$ and it decreases to 0.005$\mu m^2/sec$ under VEGFR inhibition. This is in agreement with the lower instantaneous speed measured for the ectodermal vesicles compared to the skeletogenic cells (Fig. 4C). The diffusion coefficient does not correlate with vesicle size (Fig. S1C, D), which supports active diffusion. Thus, our analyses reveal an active diffusion mode of the calcium vesicle motion in both the skeletogenic and ectodermal cells, with higher diffusion coefficient in the skeletogenic cells.

Vesicle motion is not directed toward the spicule but the vesicle speed slows down close to the spicule

Lastly, we wanted to investigate vesicle deposition in normal embryos and study vesicle motion near the spicule in this condition. Vesicle-membrane fusion is a very fast process that occurs within ~100 milliseconds[58], and therefore our temporal resolution did not allow us to detect such events. However, vesicle content deposition can last several minutes, as was shown for the vesicles that carry adhesive glycoproteins that are secreted into the lumen of the drosophila salivary gland[59, 60]. To see if we could detect such processes, we studied the directionality and speed of vesicle motion relative to the spicule and tried to infer whether the vesicles are trafficked toward the spicule and if they slow down near the spicule vicinity.

To measure vesicle motion relative to the spicule we manually marked the spicule and measured vesicle velocity toward the spicule at increasing distances from the spicule (Fig. 5A, B). The average velocity is around zero indicating random motion toward and away from the spicule, which suggests that vesicle motion is not directed towards the spicule; in other words, the spicule does not attract vesicle movement towards it. However, the average vesicle speed is significantly lower near the spicules (Fig. 5C). The vesicle speed is ~0.05µm/sec at distances of 1-2µm from the spicule, while at distances ≥8µm it increases to ~0.09µm/sec, which is the average instantaneous speed in the skeletogenic cells (Fig. 5C). Overall, vesicle velocity is not directed toward the spicules but the vesicles significantly slow down near the spicule, possibly, as they bind to it and deposit their content.

Discussion

A key requirement of biomineralizing organisms is the ability to accumulate minerals inside intracellular vesicles where the mineral is kept in an amorphous state until it is deposited into the biomineralization compartment[11, 13, 15]. Despite the key role of mineral bearing vesicles in

the biological regulation of biomineralization, very little is known about their trafficking inside the biomineralizing cells and the regulation of their dynamics and deposition. Here we studied the cellular dynamics and the motion of calcium vesicles in the cells of normal sea urchin embryos and in embryos grown under VEGFR inhibition, where skeletogenesis is blocked. Our studies reveal differences in vesicle volume and speed between the epithelial ectodermal cells and the mesenchymal skeletogenic cells that generate the skeleton. In both tissues the vesicles seem to perform an active diffusion motion, with higher diffusion coefficients in the skeletogenic cells. The motion of the vesicles is not directed toward the spicule but they seem to slow down near it, as they possibly bind and deposit the mineral. Below we discuss the possible molecular mechanisms that underlie these observations and the implications of our studies on the understanding the biological regulation of biomineralization and reproducing it in artificial systems.

Our measurements show that in both control and VEGFR inhibited embryos, the average volume of calcein stained vesicles is larger in the skeletogenic cells compared to the ectodermal cells (Fig. 3D, Dataset S1). This difference might result from different processing of the vesicle content in these two cell populations. Indeed, previous studies where calcein was added to the sea water together with another membrane impermeable dye, alexa-dextran, showed different behaviors of the dyes in the skeletogenic vs. ectodermal cells: while most of the ectoderm vesicles were stained evenly with the two dyes, about a third of the skeletogenic vesicles were stained only in calcein and lack alexa-dextran[11]. This indicates that calcium vesicles in the skeletogenic cells are biologically processed to eliminate the sea water and increase the calcium concentration, while in the ectoderm this processing does not occur. Together, these findings indicate that the biological regulation of calcium vesicle content is distinct between the skeletogenic and the ectodermal cells which apparently leads to higher calcium vesicle volume in the skeletogenic biomineralizing cells. There is a multitude of evidence of a specific activation of genes that regulate CO_3^{-2} homeostasis in the skeletogenic cells, *e.g.*, the carbonic anhydrase like-7, Caral7[17, 41], and the bicarbonate transporter, SCL4a10[61]. However, further studies are required to identify the genes responsible for the specific regulation of Ca^{+2} ions in the vesicles of the skeletogenic cells.

VEGFR inhibition increases calcium vesicle volume in both the skeletogenic and ectodermal cells (Fig. 3D). Apparently, when the skeleton doesn't form and the calcium is not sequestered into the spicule, calcium is accumulated in the sea urchin blastocoel and is taken by the cells through macropinocytosis. As VEGFR is only expressed in the skeletogenic cells, the increase of calcium

vesicle volume in both tissues supports VEGF-independent macropinocytosis as a major source of calcium accumulation in all the cells of the embryo.

The slow speed of the vesicles compared to motor-guided motion on microtubules and the good agreement of the diffusion model support an active diffusion motion in all the cells of the embryo (Fig. 4). In active diffusion motion the vesicle diffusion length depends on the mechanical properties and dynamics of the cytoskeleton network in the cells so every object in the cell is expected to move in a similar manner, regardless of its size[34, 37]. Hence, the lower speed and diffusion coefficient of the vesicles in the ectoderm could be due to the epithelial nature of these cells that makes them stiffer compared to the mesenchymal skeletogenic cells[51]. The lack of correlation between the diffusion coefficient and vesicle size (Fig. S1C,D) and the similarity of the values we measured to the diffusion coefficients measured in mice synapses where the vesicle size is much smaller (~50-100nm)[62], further support the active diffusion motion modality. Under VEGFR inhibition, the vesicle speed is slightly reduced but the vesicles continue in their diffusive motion, indicating that the motion of the vesicles in the cells is VEGF-independent. Overall, our studies suggest that calcium vesicles undergo active diffusion motion that reflects the mechanical properties of cells and therefore varies between the mesenchymal skeletogenic cells and the epithelial ectodermal cells of the sea urchin embryo.

The interaction of the embryos with the surrounding agarose could have potentially affected the mechanical properties of the cells, as environmental stiffness was shown to affect cell stiffness and mechanical properties in other systems[51]. The agarose stiffness is about 35-50kP[63] which is much more rigid than the sea water where the sea urchins naturally grow. The agarose stiffness could increase the stiffness of the ectodermal cells and of the skeletogenic cells that attach to them and affect their mechanical properties. This effect and possibly the lack of movement, could underlie the slow growth of the spicule under these conditions. Relatedly, vertebrates' endothelial cell-specification and vascular tubulogenesis were shown to depend on the mechanical properties of the substrate *in-vitro*[52, 64, 65]. Specifically, growth on soft substrates promoted VEGF-induced vascular tubulogenesis whereas growth on more rigid substrates inhibited this process[52]. It would be interesting to study the effect of environmental stiffness on the mechanical properties of the sea urchin embryonic cells and see whether the inhibition of tubulogensis in hard substrates is common to vertebrate vascularization and sea urchin skeletogenesis.

Our analysis of vesicle movement near the spicules showed that the vesicle motion is not directed towards the spicule but they slow down at distances of 1-2μm from the spicule, as they possibly

bind to it (Fig. 5). In the *Drosophila* salivary gland a regulatory network of cytoskeleton proteins assembles around the vesicles once they bind to the apical membrane and controls the secretion of the vesicle content[59, 60]. This network includes the small GTPase, Rho1, that activates the Rho kinase, ROK, that activates myosin II contractions. Additionally, Rho1 recruits a RhoGap protein that inactivates Rho1 which leads to the disassembly of the F-actin around the vesicles[60]. Relatedly, inhibition of the sea urchin homolog of ROK completely blocks skeletogenesis, inhibition of the small GTPase CDC42 prevents the formation of the spicule chord and biomineralization, and knockdown of the RhoGap gene, rhogap24l/2 perturbs normal spicule formation[17, 66, 67]. Based on these works and on our observation, we offer the following hypothesis for mineral deposition: The calcium vesicles attach to the inner membrane of the spicule chord, and secret their content by regulated acto-myosin contractions around the vesicle. To verify our hypothesis, the role of these and other cytoskeleton remodeling proteins in vesicle deposition in the sea urchin need to be investigated.

The absence of directed vesicle motion is quite promising for the design of artificial systems that try to mimic the ability of biomineralizing cells to control mineral properties and growth[5, 68]. In these systems, synthetic vesicles with controlled lipid, protein and mineral content are fabricated, the proteoliposomes. The proteoliposomes are investigated in search for novel therapeutic approaches for promoting calcification on one hand, and preventing ectopic calcification on the other hand[5, 6, 68]. If mineral bearing vesicles are not actively transported to the biomineralization site, but just diffuse, there is one less molecular mechanism to worry about when constructing artificial vesicle based biomimetic systems. Thus, our studies provide a promising starting point for deciphering the molecular control of calcium vesicle dynamics with implications for both basic and translational research.

Methods

Adult animals and embryo cultures

Adult *L. variegatus* were obtained from the Duke University Marine Laboratory (Beaufort, NC, USA). Spawning was induced by intracoelomic injection of 0.5M KCl. Embryos were cultured in artificial sea water at 23°C.

Calcein staining

A 2mg/ml stock solution of green calcein (C0875, Sigma, Japan) was prepared by dissolving the chemical in distilled water. Working solution of 25µg/ml was prepared by diluting the stock

solution in artificial sea water. Embryos were grown in calcein artificial sea water from fertilization and washed from calcein about 2-3 hours prior to the experiments.

FM4-64 staining

A 100µg/ml stock solution of FM4-64 (T13320, Life technologies, OR, USA) was prepared by dissolving the chemical in distilled water. Working solution of 5µg/ml was prepared by diluting the stock solution in artificial sea water. Calcein stained embryos were immersed in working solution about 10 minutes before visualization.

Axitinib (AG013736) treatment

A 5mM stock solution of the VEGFR inhibitor, axitinib (AG013736, Selleckchem, Houston, TX, USA), was prepared by reconstituting this chemical in dimethylsulfoxyde (DMSO). Treatments were carried out by diluting aliquots of the axitinib stock in embryo cultures to provide a final concentration of 150 nM. Control embryos in all experiments were cultured in equivalent concentrations of DMSO at no more than 0.1% (v/v).

Sample preparation for Lattice Light Sheet Microscopy

2% low melting agarose (Sigma cat# A0701) melted in artificial sea water at 37°C was added to the stained embryos at the ratio of 5:1, to immobilize the embryos. The sample was then immersed in the microscope tab with 8 mL artificial sea water with 20µL FM4-64 working solution.

Lattice Light Sheet Microscopy

The lattice light sheet microscope (LLSM) used in these experiments is housed in the Advanced Imaged Center (AIC) at the Howard Hughes Medical Institute Janelia research campus. The system is configured and operated as previously described[43]. Samples are illuminated by a 2D optical lattice generated by a spatial light modulator (SLM, Fourth Dimension Displays). The sample is excited by 488 nm, diode lasers (MPB Communications) through an excitation objective (Special Optics, 0.65 NA, 3.74-mm WD). Fluorescent emission is collected by detection objective (Nikon, CFI Apo LWD 25XW, 1.1 NA), and detected by a sCMOS camera (Hamamatsu Orca Flash 4.0 v2). Acquired data are deskewed as previously described[43] and deconvolved using an iterative Richardson-Lucy algorithm with a point-spread function empirically determined for the lattice-light sheet optical system.

Tracking of Calcium Vesicles

The automatic detection of vesicles in each frame (segmentation) is accomplished using the high-performance Hydra Image Processing library for fast 3-D image filtering[69]. We use a blob-detection approach similar to Chenourd et al. based on the Laplacian of Gaussians (LOG) filter[47]. The LOG filter can be used for blob-like object detection. In this work we used a thresholded 3D LOG to identify the vesicles in each frame. This method identifies the size and position of each vesicle, some example vesicle detections are shown in figure 3B, based on the image data in Fig. 3A. **Source code for all segmentation, tracking and statistical analyses can be found in the referenced GitLab repository[70].**

In order to keep track of each vesicle over time, we integrated our segmentation approach into the LEVER software package[48, 49]. LEVER uses a multitemporal cost function based on a small motion model to link the most likely vesicle detections into tracks (Fig. 4B). We used these vesicle tracks to analyze vesicle dynamics such as changes in velocity or size over time. The performance of the tracking algorithm degrades with significant motion, beyond the capabilities of the software to predict[48, 54]. In these datasets it is difficult to determine the frame-to-frame vesicle identities even by eye (see *e.g.* movie S7). For this reason, we have restricted our tracking-based analyses to datasets with a time-lapse of 6.12 seconds or less, per frame.

Single-Frame Manual Identification of Ectodermal Region

In order to examine the dynamics of calcium specifically in the skeletogenic cells, we must separate out the ectoderm cells which form the exterior layer of the sea urchin embryo. However, in these images, the cells of the ectodermal region are often similar in their general shape to the skeletogenic cells and are quite close together. For this task we manually defined the ectodermal boundary in the first frame of each dataset. An example of such a boundary is shown in figure 3C.

We also applied a registration algorithm using normalized covariance to automatically detect motion of the ectoderm region over time. For all movies analyzed, the motion of the ectoderm region was minimal for the first 50 frames. We therefore limited the analysis of our datasets to the first 50 frames, allowing the use of the ectoderm mask for identifying vesicles throughout the analysis.

Vesicle Speed, Directionality, and Motion

We measure the frame-to-frame speed of each vesicle by measuring the distance moved between frames divided by the frame rate. This instantaneous speed is averaged over each vesicle track to produce an **average instantaneous speed** per vesicle. Short vesicle tracks (less than 7 frames) are ignored as they are likely to be made up of noisy or unreliable detections.

We also measure the **directionality index** for each vesicle (Fig. 4B). This is the ratio of the maximal displacement of the vesicle divided by the total path length traveled by the vesicle in a window of 60 seconds. For example, in figure 4B, the directionality index ratio would be the length of the white dotted segment (maximal displacement) divided by the total length of the magenta segments. The index is related to the directedness of motion observed for each vesicle, a vesicle traveling in a straight line will have a directionality index of 1, whereas an undirected vesicle will have a low directionality index.

In order to identify the types of motions exhibited by the calcium vesicles, we fit a standard diffusion motion model to each track. For the diffusion model, we measure the **diffusion coefficient** as the slope of the linear relationship between vesicle mean-square displacement (MSD) and time. All motion and size comparisons were based on the vesicle segmentation and tracking information from the LEVER software, they were computed using MATLAB version 2019b analysis software.

Spicule-Relative Measurements

Understanding the dynamics of calcium vesicles in biomineralization requires identifying the motion of vesicles relative to the skeletal structure (spicule) in DMSO image sequences. For a selection of movies with a visually defined spicule, we manually identify the spicule centerline in a single frame. An example centerline is shown along with the 3-D spicule image in figure 5A. All vesicle distances are measured relative to the spicule centerline in each frame. Vesicles are binned in 1µm increments by their average distance from the spicule for comparison of average speed at different distances from the spicule. Average distance change per second is also measured for each vesicle, this is referred to as the average velocity toward the spicule.

Statistical Analysis

For the analysis of differences in average vesicle size and motion characteristics, we first apply the Kruskal-Wallis one-way rank test to identify if there are significant differences across all experimental groups and regions. If a significant difference is observed, then post-hoc pairwise analysis (Dunn-Sidak) is carried out between groups to identify differences between each pair of interest. The MATLAB version 2019b software package was used to perform the analysis. The p-values of each comparison are presented in Dataset S1.

References

1. Lowenstam HA, Weiner S. On Biomineralization. New York: Oxford University Press; 1989.
2. Lerch MM, Grinthal A, Aizenberg J. Viewpoint: Homeostasis as Inspiration-Toward Interactive Materials. Adv Mater. 2020:e1905554. Epub 2020/01/11. doi: 10.1002/adma.201905554. PubMed PMID: 31922621.
3. Wu F, Chen S, Chen B, Wang M, Min L, Alvarenga J, et al. Bioinspired Universal Flexible Elastomer-Based Microchannels. Small. 2018;14(18):e1702170. Epub 2018/01/13. doi: 10.1002/smll.201702170. PubMed PMID: 29325208.
4. Kumar K, Liu J, Christianson C, Ali M, Tolley MT, Aizenberg J, et al. A Biologically Inspired, Functionally Graded End Effector for Soft Robotics Applications. Soft Robot. 2017;4(4):317-23. Epub 2017/12/19. doi: 10.1089/soro.2017.0002. PubMed PMID: 29251563.
5. Simao AM, Yadav MC, Ciancaglini P, Millan JL. Proteoliposomes as matrix vesicles' biomimetics to study the initiation of skeletal mineralization. Braz J Med Biol Res. 2010;43(3):234-41. Epub 2010/04/20. doi: 10.1590/s0100-879x2010007500008. PubMed PMID: 20401430; PubMed Central PMCID: PMCPMC5298493.
6. Bolean M, Izzi B, van Kerckhoven S, Bottini M, Ramos AP, Millan JL, et al. Matrix vesicle biomimetics harboring Annexin A5 and alkaline phosphatase bind to the native collagen matrix produced by mineralizing vascular smooth muscle cells. Biochim Biophys Acta Gen Subj. 2020;1864(8):129629. Epub 2020/05/04. doi: 10.1016/j.bbagen.2020.129629. PubMed PMID: 32360152.
7. Chen Y, Feng Y, Deveaux JG, Masoud MA, Chandra FS, Chen H, et al. Biomineralization Forming Process and Bio-inspired Nanomaterials for Biomedical Application: A Review. Minerals. 2019;9(68):1-21.
8. Murdock DJ, Donoghue PC. Evolutionary origins of animal skeletal biomineralization. Cells Tissues Organs. 2011;194(2-4):98-102. Epub 2011/06/01. doi: 10.1159/000324245. PubMed PMID: 21625061.
9. Knoll AH. Biomineralization and Evolutionary History. Reviews in Mineralogy and Geochemistry. 2003;54:329-56. doi: doi:10.2113/0540329.
10. De Yoreo JJ, Gilbert PU, Sommerdijk NA, Penn RL, Whitelam S, Joester D, et al. CRYSTAL GROWTH. Crystallization by particle attachment in synthetic, biogenic, and geologic environments. Science. 2015;349(6247):aaa6760. doi: 10.1126/science.aaa6760. PubMed PMID: 26228157.
11. Vidavsky N, Addadi S, Schertel A, Ben-Ezra D, Shpigel M, Addadi L, et al. Calcium transport into the cells of the sea urchin larva in relation to spicule formation. Proc Natl Acad Sci U S A. 2016. doi: 10.1073/pnas.1612017113. PubMed PMID: 27791140; PubMed Central PMCID: PMCPMC5111655.
12. Bentov S, Brownlee C, Erez J. The role of seawater endocytosis in the biomineralization process in calcareous foraminifera. Proc Natl Acad Sci U S A. 2009;106(51):21500-4. Epub 2009/12/17. doi: 10.1073/pnas.0906636106. PubMed PMID: 20007770; PubMed Central PMCID: PMCPMC2799886.
13. Weiner S, Addadi l. Crystallization Pathways in Biomineralization. Annu Rev Mater Res. 2011;41:21-40.
14. Vidavsky N, Addadi S, Mahamid J, Shimoni E, Ben-Ezra D, Shpigel M, et al. Initial stages of calcium uptake and mineral deposition in sea urchin embryos. Proc Natl Acad Sci U S A. 2014;111(1):39-44. Epub 2013/12/18. doi: 10.1073/pnas.1312833110. PubMed PMID: 24344263; PubMed Central PMCID: PMC3890786.

581 15. Vidavsky N, Masic A, Schertel A, Weiner S, Addadi L. Mineral-bearing vesicle transport in
582 sea urchin embryos. J Struct Biol. 2015;192(3):358-65. doi: 10.1016/j.jsb.2015.09.017. PubMed
583 PMID: 26431896.
584 16. Politi Y, Metzler RA, Abrecht M, Gilbert B, Wilt FH, Sagi I, et al. Transformation
585 mechanism of amorphous calcium carbonate into calcite in the sea urchin larval spicule. Proc
586 Natl Acad Sci U S A. 2008;105(45):17362-6. Epub 2008/11/07. doi: 10.1073/pnas.0806604105.
587 PubMed PMID: 18987314; PubMed Central PMCID: PMC2582271.
588 17. Morgulis M, Gildor T, Roopin M, Sher N, Malik A, Lalzar M, et al. Possible cooption of a
589 VEGF-driven tubulogenesis program for biomineralization in echinoderms. Proc Natl Acad Sci U S
590 A. 2019. doi: 10.1073/pnas.1902126116. PubMed PMID: 31152134.
591 18. Oliveri P, Tu Q, Davidson EH. Global regulatory logic for specification of an embryonic
592 cell lineage. Proc Natl Acad Sci U S A. 2008;105(16):5955-62. Epub 2008/04/17. doi:
593 10.1073/pnas.0711220105. PubMed PMID: 18413610; PubMed Central PMCID: PMC2329687.
594 19. Gibbins JR, Tilney LG, Porter KR. Microtubules in the formation and development of the
595 primary mesenchyme in Arbacia punctulata. I. The distribution of microtubules. J Cell Biol.
596 1969;41(1):201-26. PubMed PMID: 5775786; PubMed Central PMCID: PMCPMC2107725.
597 20. Beniash E, Addadi L, Weiner S. Cellular control over spicule formation in sea urchin
598 embryos: A structural approach. J Struct Biol. 1999;125(1):50-62. Epub 1999/04/10. doi:
599 10.1006/jsbi.1998.4081. PubMed PMID: 10196116.
600 21. Gong YU, Killian CE, Olson IC, Appathurai NP, Amasino AL, Martin MC, et al. Phase
601 transitions in biogenic amorphous calcium carbonate. Proc Natl Acad Sci U S A.
602 2012;109(16):6088-93. Epub 2012/04/12. doi: 10.1073/pnas.1118085109. PubMed PMID:
603 22492931; PubMed Central PMCID: PMC3341025.
604 22. De-Leon SBT, Davidson EH. Gene regulation: Gene control network in development.
605 Annual Review of Biophysics and Biomolecular Structure. 2007;36:191-212. doi:
606 10.1146/annurev.biophys.35.040405.102002. PubMed PMID: WOS:000247773000010.
607 23. Wilt FH, Killian CE, Hamilton P, Croker L. The dynamics of secretion during sea urchin
608 embryonic skeleton formation. Exp Cell Res. 2008;314(8):1744-52. doi:
609 10.1016/j.yexcr.2008.01.036. PubMed PMID: 18355808; PubMed Central PMCID:
610 PMCPMC2444014.
611 24. Killian CE, Wilt FH. Endocytosis in primary mesenchyme cells during sea urchin larval
612 skeletogenesis. Exp Cell Res. 2017;359(1):205-14. doi: 10.1016/j.yexcr.2017.07.028. PubMed
613 PMID: 28782554.
614 25. Ingersoll EP, Wilt FH. Matrix metalloproteinase inhibitors disrupt spicule formation by
615 primary mesenchyme cells in the sea urchin embryo. Dev Biol. 1998;196(1):95-106. doi:
616 10.1006/dbio.1998.8857. PubMed PMID: 9527883.
617 26. McMahon HT, Boucrot E. Molecular mechanism and physiological functions of clathrin-
618 mediated endocytosis. Nat Rev Mol Cell Biol. 2011;12(8):517-33. Epub 2011/07/23. doi:
619 10.1038/nrm3151. PubMed PMID: 21779028.
620 27. Pollard TD, Lippincott-Schwartz J, Earnshaw WC, Johnson GT. Cell Biology. 3rd ed:
621 Elsevier Inc. ; 2017.
622 28. Parton RG, Simons K. The multiple faces of caveolae. Nat Rev Mol Cell Biol.
623 2007;8(3):185-94. Epub 2007/02/24. doi: 10.1038/nrm2122. PubMed PMID: 17318224.
624 29. Lim JP, Gleeson PA. Macropinocytosis: an endocytic pathway for internalising large
625 gulps. Immunol Cell Biol. 2011;89(8):836-43. Epub 2011/03/23. doi: 10.1038/icb.2011.20.
626 PubMed PMID: 21423264.

627 30. Kasahara K, Nakayama Y, Sato I, Ikeda K, Hoshino M, Endo T, et al. Role of Src-family
628 kinases in formation and trafficking of macropinosomes. J Cell Physiol. 2007;211(1):220-32.
629 Epub 2006/12/15. doi: 10.1002/jcp.20931. PubMed PMID: 17167779.
630 31. Racoosin EL, Swanson JA. Macropinosome maturation and fusion with tubular
631 lysosomes in macrophages. J Cell Biol. 1993;121(5):1011-20. Epub 1993/06/01. doi:
632 10.1083/jcb.121.5.1011. PubMed PMID: 8099075; PubMed Central PMCID: PMCPMC2119679.
633 32. Balint E, Lapointe D, Drissi H, van der Meijden C, Young DW, van Wijnen AJ, et al.
634 Phenotype discovery by gene expression profiling: mapping of biological processes linked to
635 BMP-2-mediated osteoblast differentiation. J Cell Biochem. 2003;89(2):401-26. Epub
636 2003/04/22. doi: 10.1002/jcb.10515. PubMed PMID: 12704803.
637 33. Verdeny-Vilanova I, Wehnekamp F, Mohan N, Sandoval Alvarez A, Borbely JS,
638 Otterstrom JJ, et al. 3D motion of vesicles along microtubules helps them to circumvent
639 obstacles in cells. J Cell Sci. 2017;130(11):1904-16. Epub 2017/04/20. doi: 10.1242/jcs.201178.
640 PubMed PMID: 28420672; PubMed Central PMCID: PMCPMC5482975.
641 34. Aaron J, Wait E, DeSantis M, Chew TL. Practical Considerations in Particle and Object
642 Tracking and Analysis. Curr Protoc Cell Biol. 2019;83(1):e88. Epub 2019/05/06. doi:
643 10.1002/cpcb.88. PubMed PMID: 31050869.
644 35. Saxton MJ, Jacobson K. Single-particle tracking: applications to membrane dynamics.
645 Annu Rev Biophys Biomol Struct. 1997;26:373-99. Epub 1997/01/01. doi:
646 10.1146/annurev.biophys.26.1.373. PubMed PMID: 9241424.
647 36. Posey D, Blaisdell-Pijuan P, Knoll SK, Saif TA, Ahmed WW. Small-scale displacement
648 fluctuations of vesicles in fibroblasts. Scientific reports. 2018;8(1):13294. Epub 2018/09/07. doi:
649 10.1038/s41598-018-31656-3. PubMed PMID: 30185883; PubMed Central PMCID:
650 PMCPMC6125338.
651 37. Brangwynne CP, Koenderink GH, MacKintosh FC, Weitz DA. Intracellular transport by
652 active diffusion. Trends Cell Biol. 2009;19(9):423-7. Epub 2009/08/25. doi:
653 10.1016/j.tcb.2009.04.004. PubMed PMID: 19699642.
654 38. Rafiq K, Shashikant T, McManus CJ, Ettensohn CA. Genome-wide analysis of the
655 skeletogenic gene regulatory network of sea urchins. Development. 2014;141(4):950-61. Epub
656 2014/02/06. doi: 10.1242/dev.105585. PubMed PMID: 24496631.
657 39. Adomako-Ankomah A, Ettensohn CA. Growth factor-mediated mesodermal cell
658 guidance and skeletogenesis during sea urchin gastrulation. Development. 2013;140(20):4214-
659 25. doi: 10.1242/dev.100479. PubMed PMID: 24026121.
660 40. Duloquin L, Lhomond G, Gache C. Localized VEGF signaling from ectoderm to
661 mesenchyme cells controls morphogenesis of the sea urchin embryo skeleton. Development.
662 2007;134(12):2293-302. Epub 2007/05/18. doi: 10.1242/dev.005108. PubMed PMID: 17507391.
663 41. Sun Z, Ettensohn CA. Signal-dependent regulation of the sea urchin skeletogenic gene
664 regulatory network. Gene Expr Patterns. 2014;16(2):93-103. doi: 10.1016/j.gep.2014.10.002.
665 PubMed PMID: 25460514.
666 42. Potente M, Gerhardt H, Carmeliet P. Basic and therapeutic aspects of angiogenesis. Cell.
667 2011;146(6):873-87. Epub 2011/09/20. doi: 10.1016/j.cell.2011.08.039. PubMed PMID:
668 21925313.
669 43. Chen BC, Legant WR, Wang K, Shao L, Milkie DE, Davidson MW, et al. Lattice light-sheet
670 microscopy: imaging molecules to embryos at high spatiotemporal resolution. Science.
671 2014;346(6208):1257998. Epub 2014/10/25. doi: 10.1126/science.1257998. PubMed PMID:
672 25342811; PubMed Central PMCID: PMCPMC4336192.

673 44. de Chaumont F, Dallongeville S, Chenouard N, Herve N, Pop S, Provoost T, et al. Icy: an
674 open bioimage informatics platform for extended reproducible research. Nat Methods.
675 2012;9(7):690-6. Epub 2012/06/30. doi: 10.1038/nmeth.2075. PubMed PMID: 22743774.
676 45. Amat F, Lemon W, Mossing DP, McDole K, Wan Y, Branson K, et al. Fast, accurate
677 reconstruction of cell lineages from large-scale fluorescence microscopy data. Nat Methods.
678 2014;11(9):951-8. Epub 2014/07/22. doi: 10.1038/nmeth.3036. PubMed PMID: 25042785.
679 46. Bray MA, Carpenter AE. CellProfiler Tracer: exploring and validating high-throughput,
680 time-lapse microscopy image data. BMC Bioinformatics. 2015;16:368. Epub 2015/11/06. doi:
681 10.1186/s12859-015-0759-x. PubMed PMID: 26537300; PubMed Central PMCID:
682 PMCPMC4634901.
683 47. Chenouard N, Smal I, de Chaumont F, Maska M, Sbalzarini IF, Gong Y, et al. Objective
684 comparison of particle tracking methods. Nat Methods. 2014;11(3):281-9. Epub 2014/01/21.
685 doi: 10.1038/nmeth.2808. PubMed PMID: 24441936; PubMed Central PMCID:
686 PMCPMC4131736.
687 48. Winter MR, Liu M, Monteleone D, Melunis J, Hershberg U, Goderie SK, et al.
688 Computational Image Analysis Reveals Intrinsic Multigenerational Differences between Anterior
689 and Posterior Cerebral Cortex Neural Progenitor Cells. Stem cell reports. 2015;5(4):609-20. Epub
690 2015/09/08. doi: 10.1016/j.stemcr.2015.08.002. PubMed PMID: 26344906; PubMed Central
691 PMCID: PMCPMC4624899.
692 49. Winter M, Mankowski W, Wait E, Temple S, Cohen AR. LEVER: software tools for
693 segmentation, tracking and lineaging of proliferating cells. Bioinformatics. 2016;32(22):3530-1.
694 Epub 2016/07/18. doi: 10.1093/bioinformatics/btw406. PubMed PMID: 27423896; PubMed
695 Central PMCID: PMCPMC5181556.
696 50. Heddleston JM, Chew TL. Light sheet microscopes: Novel imaging toolbox for visualizing
697 life's processes. Int J Biochem Cell Biol. 2016;80:119-23. Epub 2016/10/31. doi:
698 10.1016/j.biocel.2016.10.002. PubMed PMID: 27725275.
699 51. Engler AJ, Sen S, Sweeney HL, Discher DE. Matrix elasticity directs stem cell lineage
700 specification. Cell. 2006;126(4):677-89. Epub 2006/08/23. doi: 10.1016/j.cell.2006.06.044.
701 PubMed PMID: 16923388.
702 52. Hanjaya-Putra D, Yee J, Ceci D, Truitt R, Yee D, Gerecht S. Vascular endothelial growth
703 factor and substrate mechanics regulate in vitro tubulogenesis of endothelial progenitor cells. J
704 Cell Mol Med. 2010;14(10):2436-47. Epub 2009/12/09. doi: 10.1111/j.1582-4934.2009.00981.x.
705 PubMed PMID: 19968735; PubMed Central PMCID: PMCPMC3823161.
706 53. Hodor PG, Illies MR, Broadley S, Ettensohn CA. Cell-substrate interactions during sea
707 urchin gastrulation: migrating primary mesenchyme cells interact with and align extracellular
708 matrix fibers that contain ECM3, a molecule with NG2-like and multiple calcium-binding
709 domains. Dev Biol. 2000;222(1):181-94. Epub 2000/07/08. doi: 10.1006/dbio.2000.9696.
710 PubMed PMID: 10885756.
711 54. Winter MR, Fang C, Banker G, Roysam B, Cohen AR. Axonal transport analysis using
712 Multitemporal Association Tracking. Int J Comput Biol Drug Des. 2012;5(1):35-48. Epub
713 2012/03/23. doi: 10.1504/IJCBDD.2012.045950. PubMed PMID: 22436297; PubMed Central
714 PMCID: PMCPMC3380808.
715 55. Potokar M, Kreft M, Pangrsic T, Zorec R. Vesicle mobility studied in cultured astrocytes.
716 Biochem Biophys Res Commun. 2005;329(2):678-83. Epub 2005/03/02. doi:
717 10.1016/j.bbrc.2005.02.030. PubMed PMID: 15737639.
718 56. Potokar M, Kreft M, Li L, Daniel Andersson J, Pangrsic T, Chowdhury HH, et al.
719 Cytoskeleton and vesicle mobility in astrocytes. Traffic. 2007;8(1):12-20. Epub 2007/01/19. doi:
720 10.1111/j.1600-0854.2006.00509.x. PubMed PMID: 17229312.

721 57. Balint S, Verdeny Vilanova I, Sandoval Alvarez A, Lakadamyali M. Correlative live-cell and
722 superresolution microscopy reveals cargo transport dynamics at microtubule intersections. Proc
723 Natl Acad Sci U S A. 2013;110(9):3375-80. Epub 2013/02/13. doi: 10.1073/pnas.1219206110.
724 PubMed PMID: 23401534; PubMed Central PMCID: PMCPMC3587250.
725 58. Domanska MK, Kiessling V, Stein A, Fasshauer D, Tamm LK. Single vesicle millisecond
726 fusion kinetics reveals number of SNARE complexes optimal for fast SNARE-mediated membrane
727 fusion. J Biol Chem. 2009;284(46):32158-66. Epub 2009/09/18. doi: 10.1074/jbc.M109.047381.
728 PubMed PMID: 19759010; PubMed Central PMCID: PMCPMC2797286.
729 59. Rousso T, Schejter ED, Shilo BZ. Orchestrated content release from Drosophila glue-
730 protein vesicles by a contractile actomyosin network. Nat Cell Biol. 2016;18(2):181-90. Epub
731 2015/12/08. doi: 10.1038/ncb3288. PubMed PMID: 26641716.
732 60. Segal D, Zaritsky A, Schejter ED, Shilo BZ. Feedback inhibition of actin on Rho mediates
733 content release from large secretory vesicles. J Cell Biol. 2018;217(5):1815-26. Epub
734 2018/03/03. doi: 10.1083/jcb.201711006. PubMed PMID: 29496739; PubMed Central PMCID:
735 PMCPMC5940311.
736 61. Hu MY, Yan JJ, Petersen I, Himmerkus N, Bleich M, Stumpp M. A SLC4 family bicarbonate
737 transporter is critical for intracellular pH regulation and biomineralization in sea urchin embryos.
738 eLife. 2018;7. Epub 2018/05/02. doi: 10.7554/eLife.36600. PubMed PMID: 29714685; PubMed
739 Central PMCID: PMCPMC5986267.
740 62. Rothman JS, Kocsis L, Herzog E, Nusser Z, Silver RA. Physical determinants of vesicle
741 mobility and supply at a central synapse. eLife. 2016;5. Epub 2016/08/20. doi:
742 10.7554/eLife.15133. PubMed PMID: 27542193; PubMed Central PMCID: PMCPMC5025287.
743 63. Salerno M, Dante S, Patra N, Diaspro A. AFM measurement of the stiffness of layers of
744 agarose gel patterned with polylysine. Microsc Res Tech. 2010;73(10):982-90. Epub 2010/03/17.
745 doi: 10.1002/jemt.20838. PubMed PMID: 20232377.
746 64. Xue C, Zhang T, Xie X, Zhang Q, Zhang S, Zhu B, et al. Substrate stiffness regulates
747 arterial-venous differentiation of endothelial progenitor cells via the Ras/Mek pathway. Biochim
748 Biophys Acta Mol Cell Res. 2017;1864(10):1799-808. Epub 2017/07/25. doi:
749 10.1016/j.bbamcr.2017.07.006. PubMed PMID: 28732675.
750 65. Smith Q, Chan XY, Carmo AM, Trempel M, Saunders M, Gerecht S. Compliant
751 substratum guides endothelial commitment from human pluripotent stem cells. Sci Adv.
752 2017;3(5):e1602883. Epub 2017/06/06. doi: 10.1126/sciadv.1602883. PubMed PMID: 28580421;
753 PubMed Central PMCID: PMCPMC5451190.
754 66. Sepulveda-Ramirez SP, Toledo-Jacobo L, Henson JH, Shuster CB. Cdc42 controls primary
755 mesenchyme cell morphogenesis in the sea urchin embryo. Dev Biol. 2018;437(2):140-51. Epub
756 2018/03/21. doi: 10.1016/j.ydbio.2018.03.015. PubMed PMID: 29555242; PubMed Central
757 PMCID: PMCPMC5973877.
758 67. Croce J, Duloquin L, Lhomond G, McClay DR, Gache C. Frizzled5/8 is required in
759 secondary mesenchyme cells to initiate archenteron invagination during sea urchin
760 development. Development. 2006;133(3):547-57. doi: 10.1242/dev.02218. PubMed PMID:
761 16396908.
762 68. Simao AMS, Bolean M, Favarin BZ, Veschi EA, Tovani CB, Ramos AP, et al. Lipid
763 microenvironment affects the ability of proteoliposomes harboring TNAP to induce
764 mineralization without nucleators. J Bone Miner Metab. 2019;37(4):607-13. Epub 2018/10/17.
765 doi: 10.1007/s00774-018-0962-8. PubMed PMID: 30324534; PubMed Central PMCID:
766 PMCPMC6465158.

767 69. Wait E, Winter M, Cohen AR. Hydra image processor: 5-D GPU image analysis library
768 with MATLAB and python wrappers. Bioinformatics. 2019;35(24):5393-5. Epub 2019/06/27. doi:
769 10.1093/bioinformatics/btz523. PubMed PMID: 31240306.
770 70. Winter M. Source code for analyses described in "Dynamics and molecular control of
771 calcium-vesicle motion during sea urchin skeletogenesis revealed by 4D lattice-light-sheet-
772 microscopy" 2020. Available from: https://git-bioimage.coe.drexel.edu/opensource/llsm-
773 calcium-vesicles-lever.

774

775

Figures

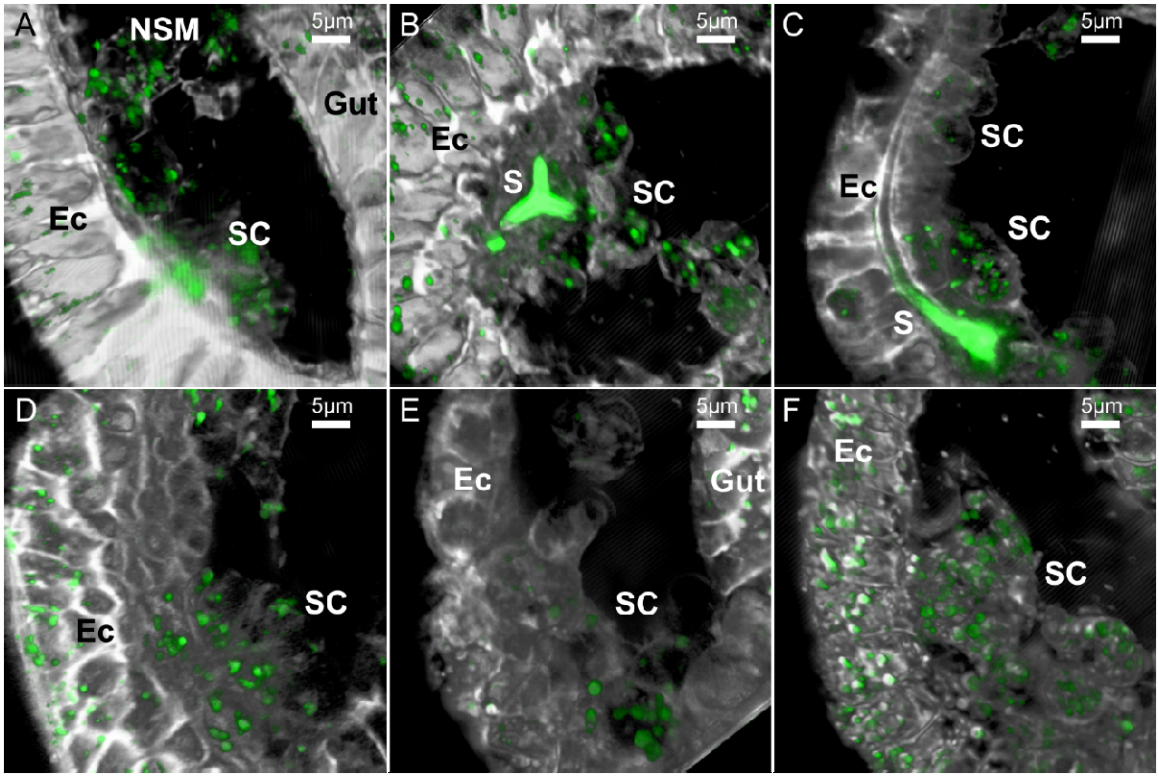

Figure 1 Examples of the LLSM 3D images of sea urchin embryos in different developmental stages and treatments. These representative images are 2D projections of the 3D rendered frames of selected datasets. Calcein staining is marked in green and the FM4-64 membrane staining is marked in gray. (A-C), control embryos (DMSO) at the early gastrula stage before spicule formation (A), just after the tri-radiate spicule forms (B) and when the spicule is elongated (C). (D-F) Representative embryos at gastrula stage treated with VEGFR inhibitor, axitinib, do not have spicules while embryos in a similar stage have elongated spicule. Scale bars are 5µm. 3D movies showing the first 100-200 frames of each of the dataset presented in this figure are provided as movies S1-6. Ec – ectoderm, SC – skeletogenic cells, NSM- non-skeletogenic mesoderm, S – spicule.

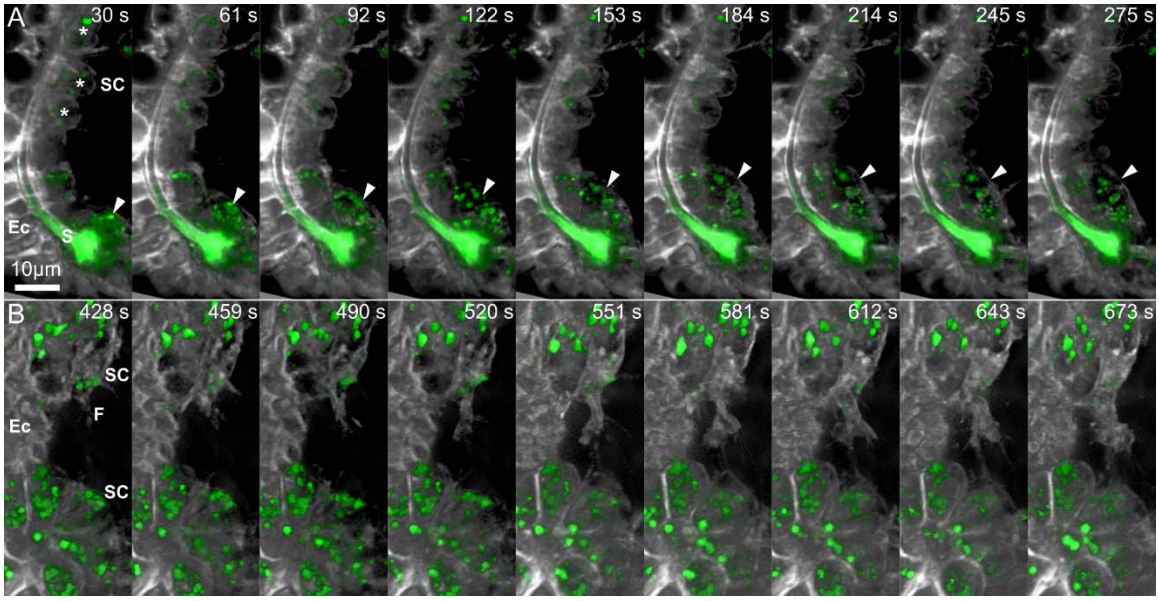

Figure 2 Sequences of time-lapse images demonstrating cellular dynamics in control and under VEGFR inhibition. (A) Time-lapse images of control embryo (sup movie 3) showing the rapid movement of a free mesenchymal cell (marked in arrowhead) compared to the stable position of the skeletogenic cells that are in direct contact with the ectoderm (asterisks). (B) Time lapse images of an embryo grown under VEGFR inhibition demonstrating the active filopodia extension and fusion between two skeletogenic cell clusters. Relative time from the beginning of the movie is shown in seconds at the top of each frame. Scale bar is 10µm. Ec – ectoderm, S – spicule, SC – skeletogenic cell, F - Filopodia.

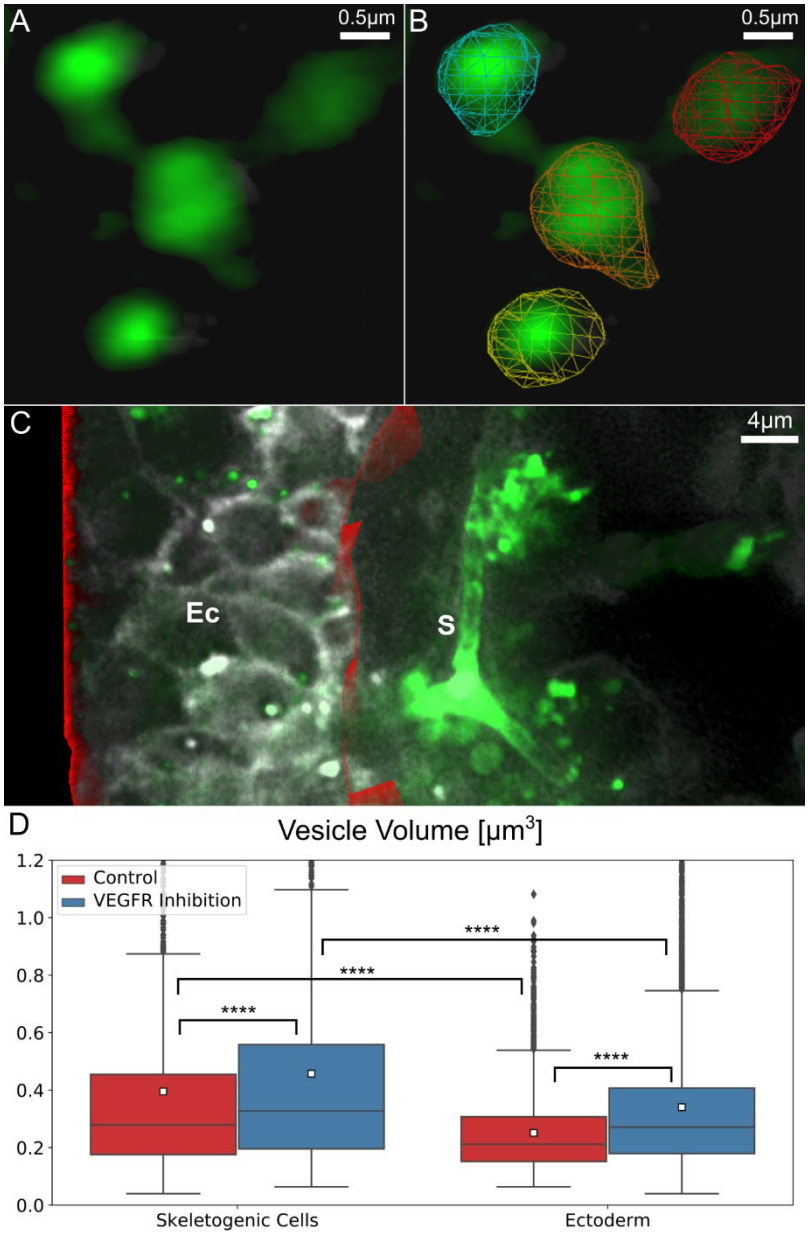

Figure 3 Vesicle volume is larger in the skeletogenic cells compared to the ectodermal cells and is significantly larger under VEGFR inhibition. (A-C) An example for the image processing involved in the quantification of vesicle volume in the ectodermal vs. skeletogenic embryonic domains. (A) Raw image rendering of calcium vesicle detection. (B) Demonstration of the automated vesicle detection (segmentation) overlaid on the image in (A). (C) Manual identification of ectodermal region in red, rendered along with raw image frame. (D) Comparison of vesicle sizes in ectodermal and skeletogenic cells in control and VEGFR inhibition. Each box plot shows the average (white square), median (middle line), the first and the third quartiles (the 25th and 75th percentiles, edges of boxes) skeletogenic cells compared to the ectodermal cells in all treatments and VEGFR inhibition significantly increases vesicle volume in the skeletogenic and the ectodermal cells. (Dunn-Sidak test, $p<0.0001$, exact p-values are given in Dataset S1).

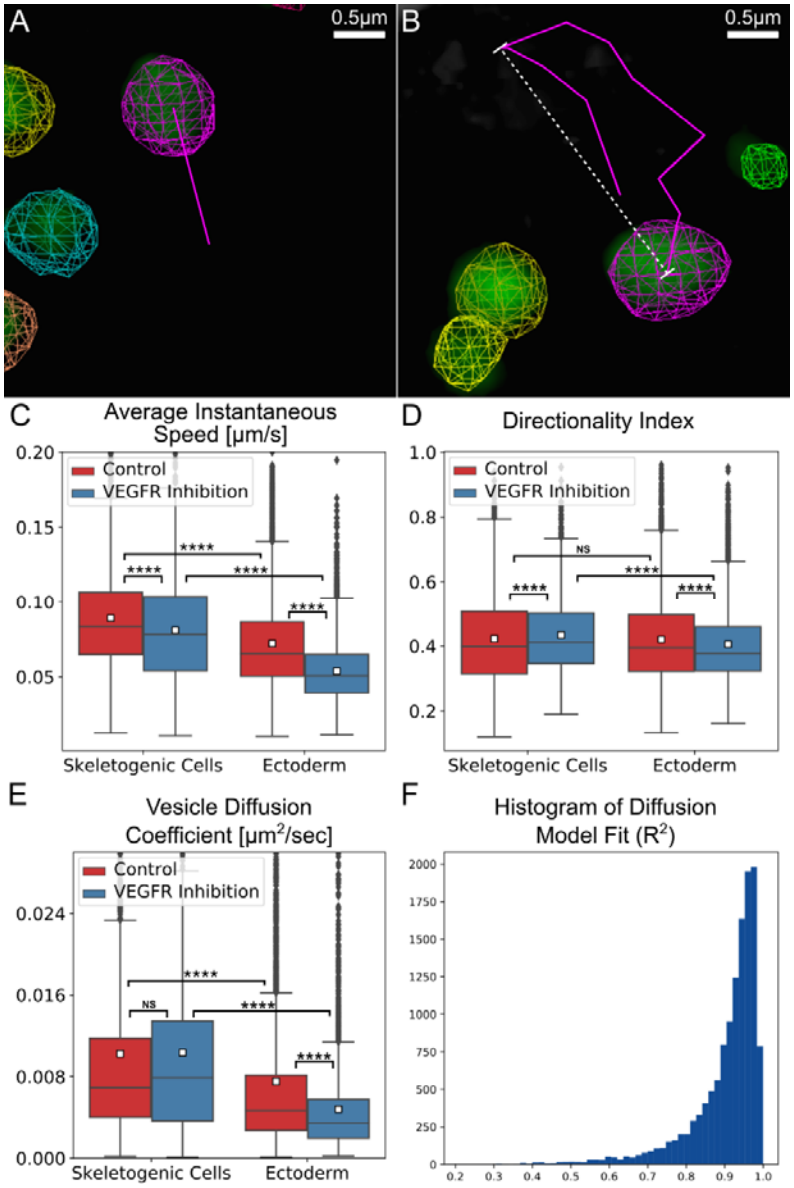

Figure 4 Vesicle tracking reveals an active diffusion motion with higher diffusion coefficient and speed in the skeletogenic cells compared to the ectodermal cells. (A, B) Examples for the automated tracking used to quantify vesicle kinetics. (A) Instantaneous speed indicates the distance traveled between sequential frames divided by the time interval between the frame. The magenta line demonstrates this distance for the magenta labeled vesicle. (B) Directionality index is the ratio of maximal displacement (white line) over the total distance traveled (magenta line) within a one-minute time interval. A representative 3D movie of tracking session is provided in movie S7. (C-E) Comparison of vesicle motion statistics between control and VEGFR inhibited embryos. Each box plot shows the average (white square), median (middle line), the first and the third quartiles (the 25th and 75th percentiles, edges of boxes) and outliers. (C) Vesicle instantaneous speed. (D) Directionality index. (E) Vesicle diffusion coefficient. (Dunn-Sidak test, $p<0.0001$, exact p-values are given in Dataset S1). (F) Histogram of Diffusion model fit, 90% of vesicle tracks are well modeled by the standard diffusion model ($R^2>0.8$).

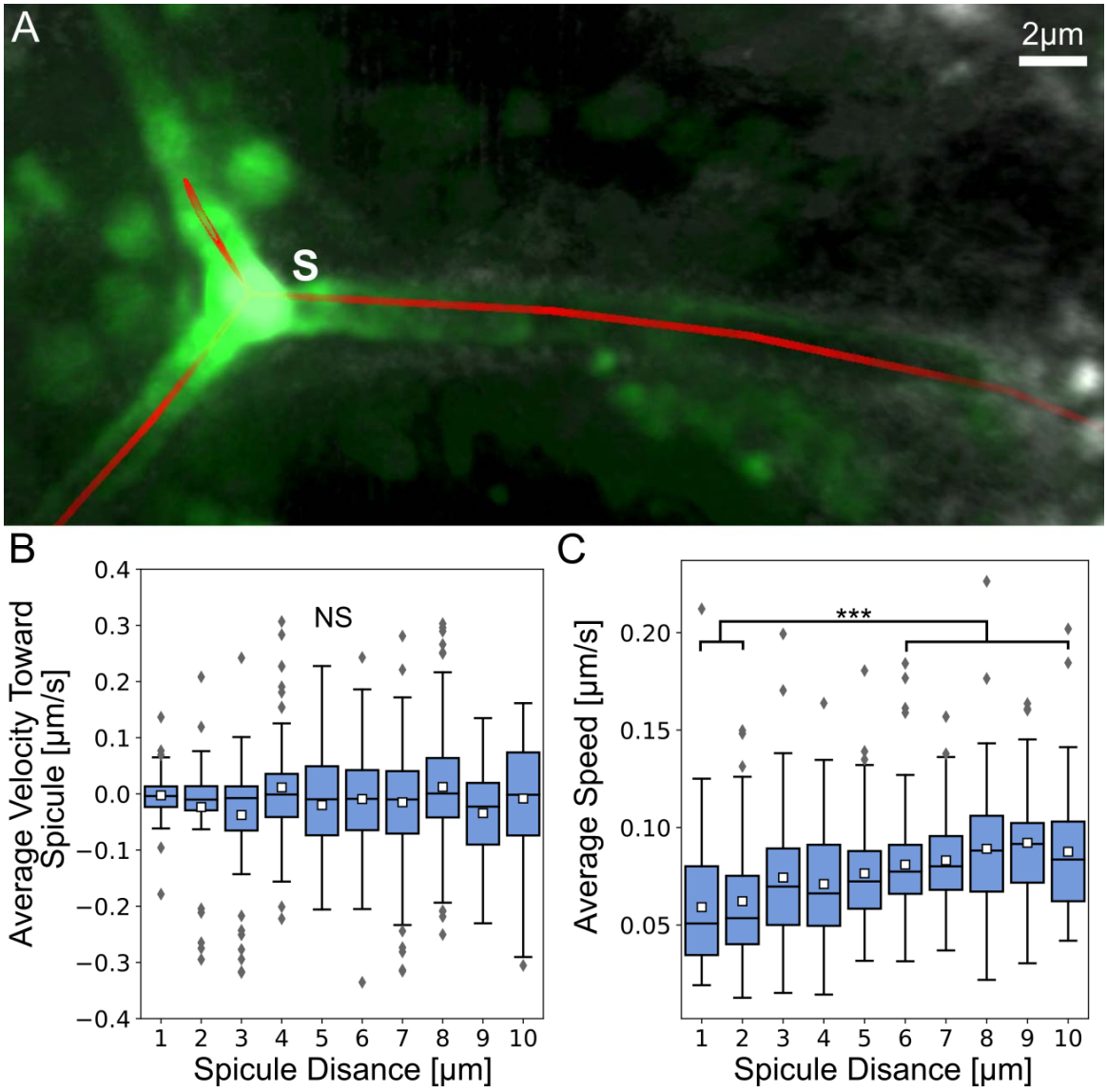

Figure 5 Vesicle velocity is not directed toward the spicule buts vesicle speed is lower near the spicule. (A) An example for the manually identified spicule centerline shown in red with raw image data. (B) Average instantaneous velocity (μm/sec) toward the spicule relative to the average distance from spicule. Each box plot shows the average (white square) median (middle line), the first and the third quartiles (the 25th and 75th percentiles, edges of boxes) and outliers. (C) Average instantaneous vesicle speed (μm/sec) at increasing average distances from the spicule (μm). The speed at distances 1-2μm are significantly lower than at distances >6μm (Dunn-Sidak test, $p<0.001$, exact p-values are given in Dataset S1).

Acknowledgements

We thank the advanced imaging center at Jenelia research campus for their instrumental help with using the LLSM and in animal maintenance. Specifically, we thank Teng-Leong Chew and John Heddleston for the help with the LLSM, Satya Kuhn for help with animals and reagents and Eric Wait for helpful discussions regarding data analysis. We thank Yarden Ben-Tabou de-Leon for the illustration of the graphical abstract. This work was supported by the Israel Science Foundation grant number 41/14 (S.B.D.), Zuckerman fellowship (M.R.W.) and ISEF fellowship (M.M.).

Author contributions

S.B.D., M.M. and T.G. designed the project. M.M. and S.B.D. performed the LLSM experiments. A.C. and M.R.W. developed visualization, tracking and segmentation tools. M.R.W. analyzed the LLSM data. S.B.D., M.R.W., M.M. and T.G. interpreted the analyses results. S.B.D. and M.R.W. wrote the paper with significant help from M.M. and T.G. and A.C.

Author information

The authors declare no competing financial interests. Correspondence and request for materials should be addressed to Smadar Ben-Tabou de-Leon (sben-tab@univ.haifa.ac.il)